THE JOURNAL OF PHYSICAL CHEMISTRY C
A JOURNAL OF THE AMERICAN CHEMICAL SOCIETY

pubs.acs.org/JPCC

Article

Anisotropy and Hybrid Heterosurface-Modulated Two-Dimensional Hydrogen Bond Network of Water

Adyasa Priyadarsini and Bhabani S. Mallik*

Cite This: J. Phys. Chem. C 2023, 127, 2544−2557

Read Online

ACCESS | Metrics & More | Article Recommendations | Supporting Information

ABSTRACT: We report the structure and dynamics of layered water structure near a bilayer heterosurface using classical molecular dynamics simulations and network graph theory. The heterosurfaces of our choice are technologically essential and well-studied hexagonal boron nitride (h-BN) and graphitic carbon nitride (g-C_3N_4). Starting with the water density distribution profile, we have studied different hydrogen bondings (HBs) associated with distance and angle distributions and correlated them with the HB count, followed by the investigations of dynamic properties. We realize the oddity while corresponding to the tetrahedral order parameter (TOP), HB donor/acceptor count, and HB lifetime. A quantitative gap is observed between the TOP and HB counts, and we perceive another structural factor playing a significant role. We observe a 2D sheetlike arrangement of hydrogen-bonded water molecules, namely, 2D-HB, in the interfacial layer instead of 3D tetrahedral arrangements. 2D-HB qualitatively acts as a key descriptor of the hydrophobicity of the interface. The probability of higher TOP among the interfacial layer water molecules is less for h-BN compared to g-C_3N_4. However, the per-water HBs for both the heterosurfaces remain indistinguishable, implying the existence of another significant physical factor related to HB. Hence, 2D-HB serves as a deciding factor. In the case of h-BN, water molecules in the first layer form extended 2D sheets compared to the second and bulk, which is not a scenario for g-C_3N_4. Following the network graph theory, we calculated the temporal evolution of the maximum number of water molecules connected in a single network. The layer 1 water molecules have slower orientational dynamics, higher HB lifetime, and consequently slower translational diffusion than layer 2 and bulk water molecules. The experimental studies suggested that the contact angle of water on h-BN can vary from 61.4 to 85.8°, higher than that of g-C_3N_4, depending on the surface stacking, support material, and exposure to air, which effectively makes h-BN more hydrophobic compared to g-C_3N_4. The interfacial water molecules have a smaller HB lifetime and a faster diffusion coefficient than g-C_3N_4. The HB lifetime of water molecules in bulk is less than that in the interface, irrespective of the surface. A slower reorientation lifetime, that is, 2.69 ps, for g-C_3N_4 interfacial water molecules is observed versus 2.20 ps for h-BN. Our results agree with the experimental observations and can help to understand the hydrophobicity of other relevant materials.

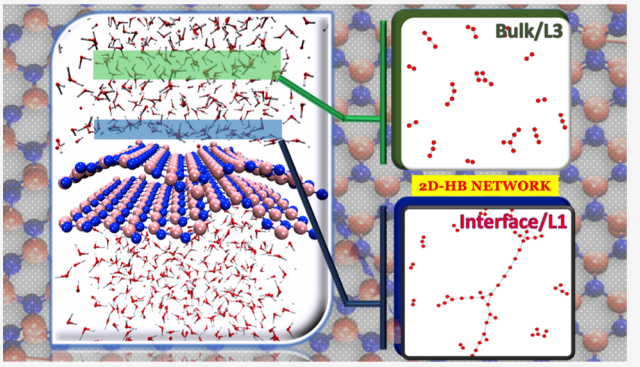

1. INTRODUCTION

Two-dimensional (2D) heterosurfaces are equipped to alter the surface chemistry, hence enhancing the catalytic ability.[1,2] Staggering advances in industrial-scale production and application of graphene and its analogous materials have been observed owing to easy and stable modulation flexibility. Hexagonal boron nitride (h-BN) and graphitic carbon nitride (g-C_3N_4) are heterosurfaces which can exist in ultrathin two dimension, the holy grail form of materials with catalytic and energy storage significance.[3−9] These heterostructures behave differently toward aqueous medium. The structural arrangement is a deciding factor in the solid−liquid interface's distinct physical and chemical phenomena. Lately, water interaction near heterosurfaces like h-BN, graphene, graphitic carbon nitride (g-C_3N_4), and Mo_2S has been gaining a lot of interest as promising candidates for technological applications like photo- and electrochemical reactions.[10−15] The wettability of the surface is detailed depending on its contact and slip angle. The wettability is directly correlated with surface hydrophobicity.[16−18] Structural and spectral arrangement of water molecules in the close interface and the difference of the same from the bulk water ones serve as the defining characteristics of a hydrophobic surface.

Evaluation of the structural orientation, the temporal evolution of dynamical properties, and hydrogen bond (HB) allied properties could be used to label hydrophobic or

Received: October 8, 2022
Revised: January 12, 2023
Published: January 26, 2023

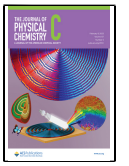

https://doi.org/10.1021/acs.jpcc.2c07098
J. Phys. Chem. C 2023, 127, 2544−2557

amphiphilic or hydrophilic surfaces. Further, using the experimental wetting angle, suggestions can be drawn regarding the hydroaffinity. Such effects have been well documented experimentally and theoretically for both h-BN and g-C_3N_4.[19,20] Graphene is treated as a trademark for hydrophobicity owing to its pure covalency, nonpolarizability, and water contact angle (WCA).[21] The graphene-like attributes of h-BN make it a proper candidate for coating and temperature-resistant material.[22−24] Recent theoretical studies suggest a significant variation in the contact angle of mono- and bilayer h-BN of 72.8 and 62.7°, respectively.[25] However, the change is insignificant for tri- and tetralayer h-BN. Another simulation study revealed a high contact angle of 86° on the h-BN monolayer.[26] Such a difference from graphene sheets is believed to be induced by the partial polarizability of the B−N bond. WCA on h-BN varies in a relatively wide range due to air exposure-induced contamination, which destroys the polarity of h-BN.[25,26] g-C_3N_4, owing to its surface polarization and corrugated sheet structure, has biocompatibility and easy functionalization.[27−29] The defect created by various % of phosphorous doping in g-C_3N_4 alters the WCA from 58.6 to 26.4°.[30] The low wettability of both surfaces was evident from recent experimental and theoretical studies using both classical and first principles molecular dynamics. Ample theoretical studies were reported with several different physical aspects to quantify the hydrophobicity of different surfaces. A comparative study among stern hydrophilic and hydrophobic sets such as graphene and SiO_2 was reported.[31] Several metal oxides were also explored to map the hydroaffinity.[32−34]

Willard and Chandler proposed an instantaneous solid−liquid interface,[35,36] where extremely structured water networks, different from bulk water, are formed. Giberti et al. detailed the proton proneness of the water layer in contact with air/vacuum and further expanded into a hydrophobic surface using the ab initio molecular dynamics simulation method.[37] The authors found very high protonphilicity of water surface vicinal to air and correlated the same with a specific kind of hydrogen-bonded orientation of water molecules. The topology was named "proton wire," which lays parallel to the surface, analogous to the tetrahedral directional water arrangement of water molecules termed "water wires."[37] The water surface refers to the topmost water layer in contact with the air. The proton wire terminology suggests proton trapping by slowing its dynamics.[36] The authors directly compared water−air contact to hydrophobic surfaces, where the proton diffusion channel runs lateral to the instantaneous heterosurface arrangement.[38] Pezzotti et al. characterized the hydrogen-bonded water channel in the air−water and hydrophobic surface−water interfaces as the two-dimensional hydrogen bond (2D-HB) network. Willard and Chandler's model hinted at the dangling OH bond toward the surface and another involved in the strong intralayer hydrogen bonding, and later vSFG[39] or HD-SFG study reinforced the three-body interaction in the interfacial layer as there are no low-frequency bands in the spectra.[40] Skinner et al. interpreted the vSFG signal in terms of the number of HBs donated/accepted and inferred separated pairs of type 4D−2S, 2S−4D, 4D−4D, and 3D−4D, which were responsible for the vSFG spectrum.[41] However, the authors did not provide any specifications for the thickness of the interfacial layer responsible for vSFG. Later Pezotti et al. reported that the active layer was only 2−3 Å.[42] Following AIMD simulations, the authors demonstrated that the thin topmost water layer contains an extended 2D-HB network with the participation of 70% water molecules. The appearance of the small peak of low-frequency spectra, which was debated and dismissed by earlier studies,[43,44] was addressed by Pezotti et al. as of structural origin, and the 2D-HB network was responsible.[42] In few of our recent studies, we investigated structural, dynamic, and spectral properties with the static HB formation associated with water molecules interfacing bilayer BP and Gr@g-C_3N_4.[45,46] Our motive is to draw a better understanding by associating all possible physical features and set a model for hydroaffinity. Contact angle modeling requires a large set of water molecules on an expanded sheet[47−49] and provides ambiguous results regarding the hydroaffinity of the specific heterostructure. Due to the discrepancy of experimentally measured contact angles, it is difficult to theoretically rationalize and compare the hydrophobicity of a novel material on a large scale. The 3D tetrahedral arrangement is a characteristic of bulk water and affects its physical and chemical properties. However, the dangling OH bond has been universally considered the hallmark of hydrophobicity,[50] which is recently challenged as a specific locality of hydrophilic heterosurfaces, such as silica dangling OH bonds.[51] Now, the requirement emerges for another physical property that can serve as the marker for hydrophobicity.

Here, we have discussed the layer-wise distinction of physical properties of water molecules near the bilayer interface; those collectively set the ground for 2D-HB. The surface polarity of h-BN and the hydrophilic and hydrophobic localities of g-C_3N_4 are perfect candidates to initiate the comparative hydrogen-bonding study. Once we found the density-controlled sections of the surface, we performed the structural analysis, most notably the tetrahedral order parameter (TOP), directly associated with a 3D-HB motif. However, the significant loss in tetrahedrality in the interfacial layer of h-BN compared to the bulk does not tone with the loss of HB donor/acceptor count. In our previous studies,[45,52] we found that the TOP and per water HB count follow the same trend. However, they do not complement each other quantitatively. Thus, we further attend to 2D-HB to trace the effect of heterosurface. We detailed the probability of lateral orientation of water molecules. Following network graph theory, we calculated the temporal evolution of the maximum number of water molecules connected in a single network. Then, the properties are correlated with the hydrophobicity of h-BN and g-C_3N_4. Following this, we calculated the HB donor/acceptor count in the total, interlayer, and intralayer regions. The survival interval of water molecules close to L1 is significantly higher in g-C_3N_4. To append the missing links, we looked at the HB structure in the h-BN and g-C_3N_4 interfaces as they are not tetrahedrally arranged. A 2D hydrogen-bonded noninterrupted motif is found, made up of water molecules hydrogen-bonded to each other. Recently, extended 2D motifs were proposed and properly enquired upon for the water molecules in contact with instantaneous air.[42] Authors have carefully cleaved the liquid−vapor interface using Willard and Chandler's instantaneous surface model, which defined the interface and the density of water along the surface's normal direction properly.[53] The authors found 70% of water molecules on average near the air−water interface, which is a part of the extended 2D sheet, termed as the "topmost skin."[42] The same idea was later extended to trace the local hydrophobicity of a

https://doi.org/10.1021/acs.jpcc.2c07098
J. Phys. Chem. C 2023, 127, 2544−2557

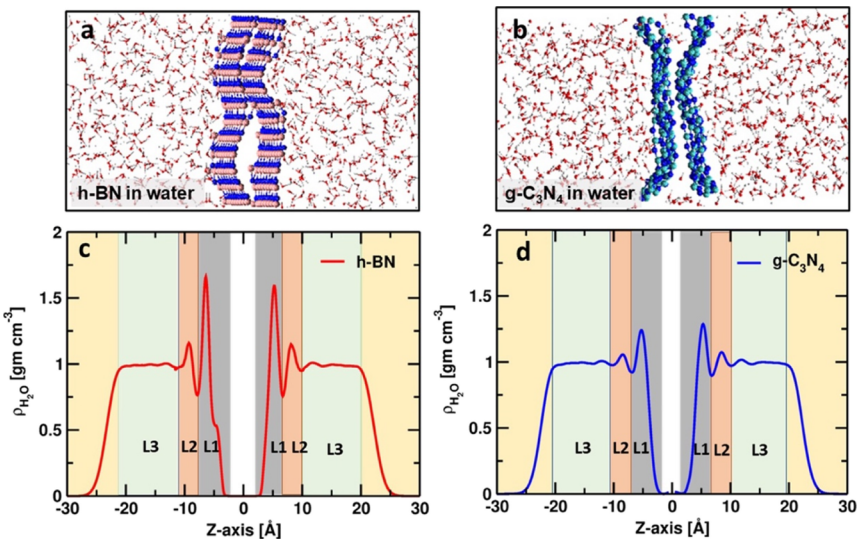

Figure 1. Density profile of water molecules distributed along the *z*-axis of the simulation box around (a) h-BN and (b) g-C_3N_4. The distinctions between layer 1, layer 2, and layer 3 are depicted by gray, orange, and green patches, respectively.

rather common hydrophilic surface.[54] We observe the expanse of the 2D sheetlike motif for the h-BN interface compared to other layers and all water layers around g-C_3N_4 as well. A fitting correlation is found among all mentioned properties.

2. COMPUTATIONAL DETAILS

We performed classical molecular dynamics simulations to study the interaction between heterosurface and water molecules. The bilayer heterosurfaces were generated and initially simulated using VASP for energy minimization purposes. The h-BN and g-C_3N_4 surfaces consist of 11 × 10 and 3 × 4 supercells, respectively. Once the energy was minimized, presimulated water boxes were added along both sides of the bilayer surface. We kept the surface dimension similar for both systems. Hence, we used a water box of 23 × 25 × 23 Å^3, making the total dimension of the box 23 × 25 × 80 Å^3 with a total of 780 water molecules in the system, maintaining experimental water density, that is, 1 gm cm^{-3}. The simulation boxes are pictorially depicted in Figure 1a,b. The classical simulations were performed using the large-scale atomic/molecular massively parallel simulator (LAMMPS) package.[55] The classical force field (FF) parameters are of massive importance while simulating solid surfaces and must be tuned properly according to the requirement of the interaction. The inadequacy of conventional GAFF[56,57] and OPLS[58,59] has made chemists find more appropriate parameters where both short- and long-range bonded interactions can be modeled properly. One such tried and tested FF is Tersoff,[60,61] which we used for h-BN and g-C_3N_4 intralayer or uniplanar interactions. Water molecules were simulated using the SPC/E rigid model.[62] The nonbonded interactions among sheet elements and water molecules were modeled using previously reported distance (σ_{LJ}) and energy (ϵ_{LJ}) parameters,[63−65] obtained using Lorentz−Berthelot[66,67] mixing rule, that is, $\sigma_{ij} = 1/2[\sigma_{ii} + \sigma_{jj}]$ and $\epsilon_{ij} = \sqrt{\epsilon_{ii}\epsilon_{jj}}$. The h-BN and water interactions were taken from the previously reported parameters for water permeability check through h-BN nanotube with σ_{BO} and σ_{NO} = 3.310 and 3.266 Å and ϵ_{BO} and ϵ_{NO} = 0.1214 and 0.1500 kcal mol^{-1}, respectively.[64] The partial charge values used for B and N atoms are +0.37/−0.37.[64] For g−C_3N_4−water interactions, we used the previously reported parameters, including the charge variation over g-C_3N_4.[45] As the bilayer was simulated beforehand, with both the parallel sheets flexible, during the entire simulation with water molecules, both the layers of h-BN and g-C_3N_4 were kept static, and the water molecules were arranged according to the instantaneous surface. The energy minimization was performed for h-BN-water and g−C_3N_4−water systems using the conjugate gradient method. We performed statistical sampling at 300 K using NVT simulations for 20 ns followed by 50 ns of NVE simulations. The integration step was 1 fs. The system temperature was controlled using the Nosé-Hoover thermostat,[68−70] and the SHAKE algorithm[71] was used to constrain the bond involving hydrogen atoms. All properties reported here were calculated from the trajectories generated with the NVE ensemble.

3. RESULTS AND DISCUSSION

3.1. Structure of Interface. We started with identifying the interfacial layer and the effect of the heterosurface on the same. The average density of water molecules along the *z*-axis was calculated using the widely accepted formula

$$\rho(z) = \frac{\left\langle N\left(z - \frac{\Delta z}{2}, z + \frac{\Delta z}{2}\right)\right\rangle}{L_x L_y \Delta z}$$

where $N(z - \Delta z/2, z + \Delta z/2)$ is the total number of the center of mass of water molecules in the volume, $L_xL_y\Delta z$,where Δz is the bin width of 0.1 Å. As our setup consists of a bilayer dipped in a solvent (water), we obtained water distribution along the *z*-axis in both directions, namely, 'top' for $z > 0$ Å and 'bottom' for $z < 0$ Å. A distinction between density-dependent water layers is crucial for surface-dependent interfacial studies. We have shown the snapshots of the simulations in Figure 1a,b. We identified three sets of layers, namely, layer 1 (L1, gray region), layer 2 (L2, red region), and layer 3 (L3, green region), distributed on both sides of h-BN and g-C_3N_4 as depicted in Figure 1c,d, respectively. A rigorous distinction of the interfacial, diffusion, and bulk layers was performed and followed for every physical property calculation.

https://doi.org/10.1021/acs.jpcc.2c07098
J. Phys. Chem. C 2023, 127, 2544−2557

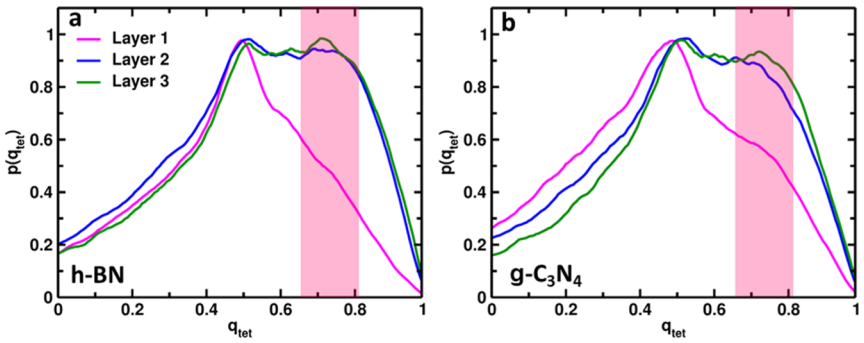

Figure 2. TOP (q_{tet}) of water molecules in the L1 (magenta line), L2 (blue line), and L3 (green line) layers distributed along (a) h-BN and (b) g-C_3N_4 surfaces.

The water density attains equivalent maxima in both the top and bottom regions of bilayer h-BN and g-C_3N_4, with average values of 1.65 and 1.25 gm cm^{-3} in L1, respectively. The second maximum, first, and second minima appear at the same distances from the first maximum in the top and bottom regions for a specific heterosurface. The relatively higher value of maximum water density is observed in the L1 of h-BN and g-C_3N_4, the reason for which we believe is two-fold: structural and chemical. Experimental observations showed that h-BN, with 85.8° contact angle, is more hydrophobic than g-C_3N_4, which has a contact angle of 58.6°.[26,30] The hydrophobicity of the heterosurface directly impacts the structural and orientational alterations. The second factor is the structural integrity of the heterosurface. Both hydrophobic and hydrophilic surfaces show a heightened maximum density in L1. However, the deciding factor for the peak height is the smoothness of the 2D surface. The smoother surfaces like graphene, h-BN, and Mo_2S show higher maximum density as compared to more corrugated surfaces like hydroxylated silica and alumina.[54] Hence, the difference in the maximum density for h-BN and g-C_3N_4 pans out as the 2D structural homogeneity effect. h-BN being more homogeneous along the 2D shows 1.65 gm cm^{-3} maximum water density in L1, which is 1.3 times the same in the case of g-C_3N_4.

3.2. Hydrogen Bond Statistics. From the P(r_{O1}) plot, depicted in Figure S1, we could not distinguish any significant difference in the peak positions for L1, L2, and L3. On the way to the HB study, the most consequential static structural property is tetrahedrality. We analyzed $P(r_{O4})$ versus r_{O4} as a prestudy of the TOP. r_{O4} defines the average distance between the central water molecule and its four nearest neighboring water molecules. The deviation in the maximum probable peak position is blue-shifted toward a higher average distance value for L1 water molecules compared to L2 and L3/bulk, irrespective of the surface under observation. However, the $P(r_{O4})$ distribution has a wider distribution for L1 water molecules close to h-BN and the highest average distance for the most probable r_{O4}. Deviation of the peak position and stretch of the plot width is utmost for L1 water molecules closest to the h-BN interface, as depicted in Supporting Information Figure S1b,f. Hence, r_{O4} has an immediate effect on the TOP (q_{tet}) calculated using the equation

$$q_{tet} = 1 - {}^{3}/_{8} \sum_{i=1}^{3} \sum_{j=i+1}^{4} (\cos\theta_{ij} + {}^{1}/_{3})$$

where θ_{ij} = the angle between ith, central, and a jth water molecules and i and j are the closest neighbors to the central water molecule.[72] As q_{tet} simply depends upon the angle formed by oxygen of the three closest water molecules, a perfect tetrahedral arrangement involving five water molecules provides a value of 1, and an utterly out-of-order set gives a value of 0. Comparing the $P(q_{tet})$ plot of L1, L2, and L3, we find that the peak in the region $q_{tet} > 0.5$ is absent for the water molecules in the L1 of h-BN and g-C_3N_4, though we find a prominent shoulder in the same region for the interfacial water molecules of g-C_3N_4. The results hint at a complete loss of the tetrahedral arrangement of hydrogen-bonded water molecules in the L1 of h-BN. In the case of g-C_3N_4, few water molecules close to the surface still maintain tetrahedrality; however, the condition is less probable than L2 and L3. Pictorially the high tetrahedrality range is depicted through a pink patch in Figure 2. The loss of tetrahedrality is common for both h-BN and g-C_3N_4.

The concept of tetrahedrality is linked to both orientational and translational order. Orientational and translational order properties are related to the angular and radial variance, respectively. Introduced by Errington and Debenedetti as a measure of tetrahedrality, translational order (t) measures the "preferential separation tendency" of the water molecules.[72] The value of t depends on the spatial arrangement of similar atoms and can be measured for noninteracting ideal gas to categorically arranged metal.[73,74] It is particularly dependent on the pressure and varies due to compression and expansion. Water molecules' hydrogen bonding is assumed to be the sole determinant of both q and t. However, recently, Duboué-Dijon et al. suggested a substitute for t, translational tetrahedral order (TTO), specifically defined for water. The TTO is defined as a function of the radial distance between central water and closest peripheral water molecules,[75] given as $S_k = 1 - \frac{1}{3}\sum_{k=1}^{4} \frac{(r_k - \bar{r})^2}{4\bar{r}^2}$. When tetrahedrality increases in the local vicinity, S_k increases. The major difference between t and S_k is that the earlier requires average structure calculation and the latter requires instantaneous structure calculation. S_k values calculated for the bulk water simulated at 298 and 260 K are 0.999000 and 0.999171 using the TIP4P/2005 FF parameter.[75] The authors observed a significant change in the orientational tetrahedral order (q) when the simulation temperature changed; however, the variation in t is quite insignificant in the order of 10^{-4}, that is, ∼0.0002. We also calculated the S_k value for L1, L2, and L3/bulk of h-BN and g-C_3N_4. For h-BN, the S_k value for L1, L2, and L3 is 0.903, 0.908, and 0.909, respectively. The translational order of L1 is less than that of L3, and the change is of the order of 10^{-4}. For g-C_3N_4, the S_k value for L1, L2, and L3 is 0.906, 0.908, and

https://doi.org/10.1021/acs.jpcc.2c07098
J. Phys. Chem. C 2023, 127, 2544−2557

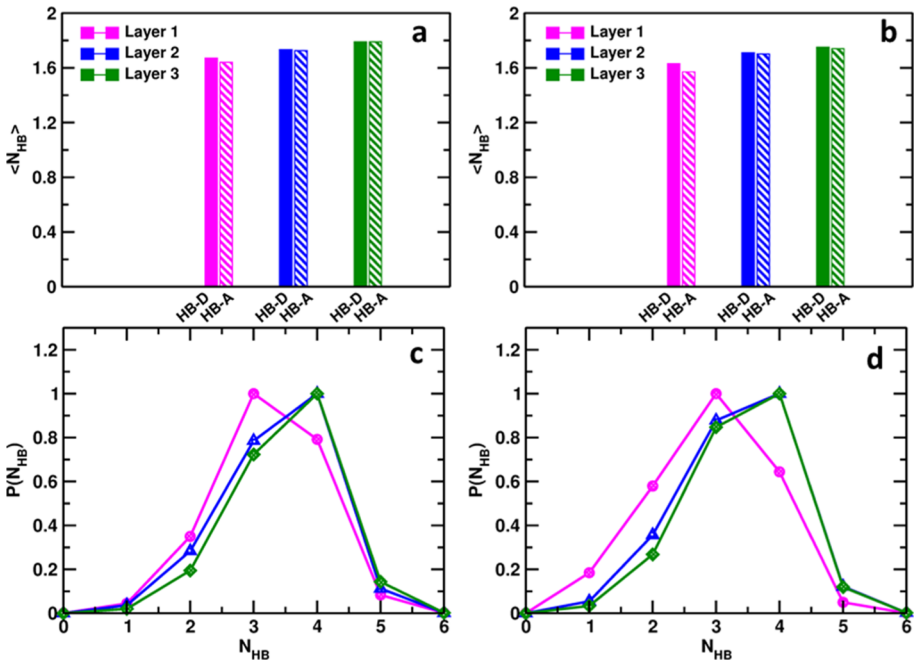

Figure 3. (a,b) represent the average numbers of HBs donated (HB-D) and accepted (HB-A) by water molecules in the different layers. (c,d) Distribution of HBs per water molecule in layer 1 (magenta), layer 2 (blue), and layer 3 (green) around h-BN and g-C_3N_4, respectively.

0.909, respectively. The reduced TTO for the h-BN interfacial water molecules is the outcome of extended 2D-HB formed between L1 water molecules. In further discussions, the relation between the TOP and hydrogen bonding will be drawn and eventually linked to the hydrophobicity of the heterosurface.

We further ventured into the likelihood of HB formation in the distinct layers. The statistically averaged HB number was calculated in two distinct formats: HB donor/acceptor (HB-D/A) count and probability distribution of per water HBs [$P(N_{HB})$]. Galli and co-workers' bond distance and angle criteria[76] were chosen to define hydrogen bonding, that is, r_{OH} < 2.45 Å and <H−O_{donor}−$O_{acceptor}$ < 30°. Figure 3a,b depicts the average number of HBs donated (HB-D) and accepted (HB-A) per water molecule. HB among water molecules in the same layer and different layers are termed intralayer and interlayer HBs. In the current discussion, we have considered total, that is, the integration of inter and intralayer hydrogen bonding. We find a decreasing number of HB-D and HB-A as we move across the water layers from L3/bulk to the L1/interfacial layer. In the L3, the total numbers of HBs formed per water layer are 3.6 and 3.5 for the h-BN and g-C_3N_4 heterosystems, respectively, which are close enough and mimic previously reported data.[42,77,78] In the interfacial layer of both the systems, the integration of HB-D and HB-A turns out to be 3.2 (h-BN) and 3.3 (g-C_3N_4), respectively. There is a decrease in the average number of HBs per water molecule as well as a loss of tetrahedrality in the L1, despite most water-dense regions. Experimental studies reveal that g-C_3N_4 and h-BN surfaces have a contact angle of 58.6 and 85.8°, respectively, which makes h-BN more hydrophobic.[26,30] In our recent classical molecular dynamics study, we revealed the amphiphilic nature of graphene and g-C_3N_4 hybrid surfaces as well as local hydrophilicity and hydrophobicity.[45] The first principles simulations revealed that the edge and defect N centers of g-C_3N_4 are locally hydrophilic and the carbon centers are hydrophobic.[79,80] A previous study comparing the structural properties of water molecules confined within the two layers of h-BN and graphene also found reduced HBs in the interfacial region by studying the continuous HB profile along the *z*-axis.[78] The same pattern is also observed in the interfacial layer of h-BN and g-C_3N_4 in our case. The effect of the heterosurface is felt on the second layer also, which leads to the reduction of the total average HBs (3.4) in the L2 compared to L3. Another significant remark we find is that the HB-D number is higher than HB-A in the L1 for both cases, whereas the values remain equivalent in the L2 and L3. We extended the static HB number calculation to the probability distribution of N_{HB}, which is the total number of HBs formed per water molecule. For the L1 water molecules, we find that maximum water molecules prefer to form three HBs, whereas for L2 and L3, N_{HB} peaks for four HBs. Comparing h-BN and g-C_3N_4, we find the deviation of the $P(N_{HB})$ for N_{HB} = 1/2/3/4 is relatively higher for g-C_3N_4 compared to h-BN. In our previous studies, we find HB counts follow the trend of TOP of water molecules in different layers. However, comparing the hydrophobicity of two heterosurfaces, we find a shoulder appearing in the region q_{tet} > 0.5 for L1 water molecules in the g−C_3N_4−water system, which is missing otherwise. The substantial loss of tetrahedrality suggests that the L1 water molecules are unable to form four HBs arranged in a tetrahedron in the case of h-BN. Hence, we conclude that the TOP of h-BN interfacial water molecules deviates maximum from the ideal condition, that is, the TOP of L3/bulk water molecules. However, we find the probability of N_{HB} = 4 is ∼10% higher for h-BN [$P(N_{HB} = 4) = 0.8$] compared to g-C_3N_4 [$P(N_{HB} = 4) = 0.64$]. The average numbers of hydrogen bonds formed per water molecule are 3.23, 3.39, and 3.50 for L1, L2, and L3 of h-BN and 2.91, 3.33, and 3.44 for L1, L2, and L3 of g-C_3N_4. For g-C_3N_4, per water HBs in L1 deviate maximum from L3/bulk values compared to BN, which is an opposite trend to TOP, suggesting the true nature of HB among L1. Though not tetrahedrally arranged, the hydrogen-bonded water clusters in the interfacial layer of h-BN are of

https://doi.org/10.1021/acs.jpcc.2c07098
J. Phys. Chem. C 2023, 127, 2544−2557

higher order in terms of the number set against g-C_3N_4. Now, the query arises of how these results can be correlated with hydrophobicity.

Before venturing further into other properties, we analyze the dynamic properties, such as survival interval, orientation autocorrelation function (OACF), HB lifetime (HBLT), and mean squared displacement (MSD), which are further correlated with the spectral properties.

In the following section, we have added the survival interval of water molecules in the L1 of h-BN and g-C_3N_4 using the formula

$$s_R(t) = \frac{\langle s(0)\cdot S(t)\rangle}{\langle (s(0))^2\rangle}$$

where $S_R(t)$ represents the continuous survival span of water molecules in the interfacial layer. $S(t)$ can be 1 if a water molecule continuously stays in L1 from $t = 0$ to time t, and it is zero otherwise, and $s(t)$ is unity when a water molecule stays in that layer at a specific time t and zero otherwise. The L1 range for h-BN and g-C_3N_4 is the same as that we previously followed. A previous FPMD study has reported that water molecules have a longer survival interval closer to the relatively less hydrophobic heterosurface.[22] Our results, pictorially depicted in Figure 4a, also hint at a longer survival span of water molecules closer to g-C_3N_4 (τ_S = 35.9 ps) compared to h-BN (τ_S = 29.9 ps).

If not tetrahedron or a three-dimensional arrangement, what could be the spatial arrangement of hydrogen-bonded water in the interfacial layer of h-BN and g-C_3N_4? Figure 4b represents the HB-D count per water molecule (N_{HB-D}) in the adjacent interface layer of h-BN and g-C_3N_4. Intralayer HBs are formed among the water molecules within the L1, and interlayer HBs

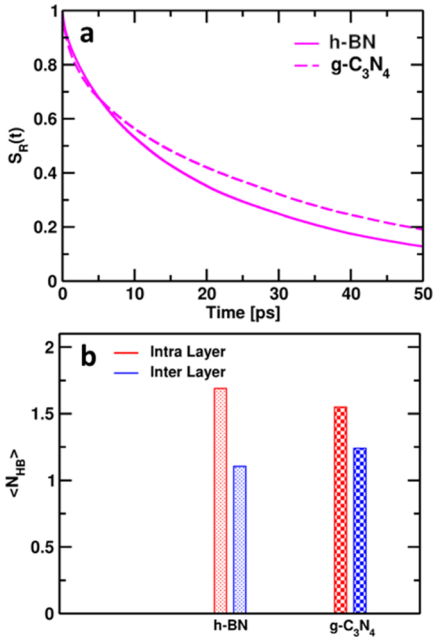

Figure 4. (a) Exponentially decaying function representing the temporal evolution of the survival interval of layer 1 (L1) water molecules in the h-BN (solid line) and g-C_3N_4 (dotted line) interface. (b) Number of HBs donated per water molecule to the water molecules in the same layer, that is, intralayer (red bars) HBs, and to the water molecules outside the same layer, that is, interlayer (blue bars) HBs.

are formed between L1 and adjacent layer water molecules. For h-BN, we find that intralayer N_{HB-D} is higher than g-C_3N_4, while the situation is contrary for interlayer N_{HB-D} values. The fact still presented a hint at a higher ordering of h-BN interfacial water molecules, and the deciding factor is assumed to be the hydrophobicity of h-BN. For g-C_3N_4, the difference in the inter- and intralayer HBs is less, suggesting that L1 water molecules prefer both L1 and L2 water molecules for HB formation. However, h-BN adjacent water layers prefer intralayer HB formation to a considerable extent compared to interlayer ones. The above discussion reproves the observations from TOP. Thus, we started digging deeper into the spatial orientation of the HBs.

3.3. 2-Dimensional Hydrogen Bonding. We started an in-depth analysis of the HB formed by L1/interfacial water molecules with the orientation of their dipole moment and angular orientation of the O−O nonbonded vector of two HB interacting water molecules. The two- or three-dimensionality of the hydrogen-bonded water clusters can be identified by observing different angular orientations to the normal vector either parallel or perpendicular to the heterostructure. To study the orientation of the water dipole moment, we calculated the projection of the <H−O−H bisector onto the vector normal to the surface (p_z). We segregated the spatial orientation of water as "UP" for $p_z \geq 0.33$, "PAR" for $-0.33 > p_z > 0.33$, and "DOWN" for $p_z \leq -0.33$. Once segregated, we calculated each set's number probability and depicted the same in Figure 5. Pezzotti et al. have tested many different p_z cutoffs and finally settled for 0.33[42]. For h-BN, the parallel orientation "PAR" has maximum probability with 44% of the dipole moment of L1 water molecules oriented parallel to the surface. In contrast, only 27 and 29% belong to the "UP" and "DOWN" categories. For g-C_3N_4, the "UP," "PAR," and "DOWN" oriented water molecules are 30, 37, and 33%. Hence, for h-BN, many water molecules in the L1 remain parallel to the instantaneous heterosurface. Though the "PAR" orientation percentage is high for g-C_3N_4 compared to "UP" and "DOWN" orientation, the number and deviation are conspicuously smaller than h-BN. Considering L2 and L3 for both h-BN and g-C_3N_4 systems, the "UP" and "DOWN" orientation surpasses the "PAR" orientation, which we think is the factor contributing to the high TOP of L2 and L3.

Later, we proceed to O−O nonbonded vector where the oxygens belong to a pair of hydrogen-bonded water molecules. In Figure 6 we have presented the scatter plot of O−O spatial distance against the cosine of the angle made by the $O_{donor}-O_{acceptor}$ vector with the unit vector normal to the surface. Figure 6a,b, and 6c depicts the distribution plots for L1, L2, and L3 water molecules around h-BN. In the interfacial layer/L1, the O−O nonbonded vectors are accumulated from 2.65 to 2.90 Å with maximum probable angular orientation perpendicular to the normal unit vector to the surface and hence parallel to the surface. However, for L2 and L3, the same distance-angle distribution can be found to be outspread in the whole angular region for the most probable O−O distance range of 2.60−2.85 Å. The distance range reiterates our $P(r_{O4})$ versus r_{O4} distribution for the h-BN interfacial water molecules. Hence, it is understandable that the water molecules located in L1 form rather long HBs. Observing the same property for g-C_3N_4 interfacial and bulk water molecules, depicted in Figure 6d−f, we find the most likely O−O distance acquires the same range in L1, L2, and L3. Comparing h-BN and g-C_3N_4 for L1 water molecules, the O_{donor} to $O_{acceptor}$ vector is oriented

https://doi.org/10.1021/acs.jpcc.2c07098
J. Phys. Chem. C 2023, 127, 2544−2557

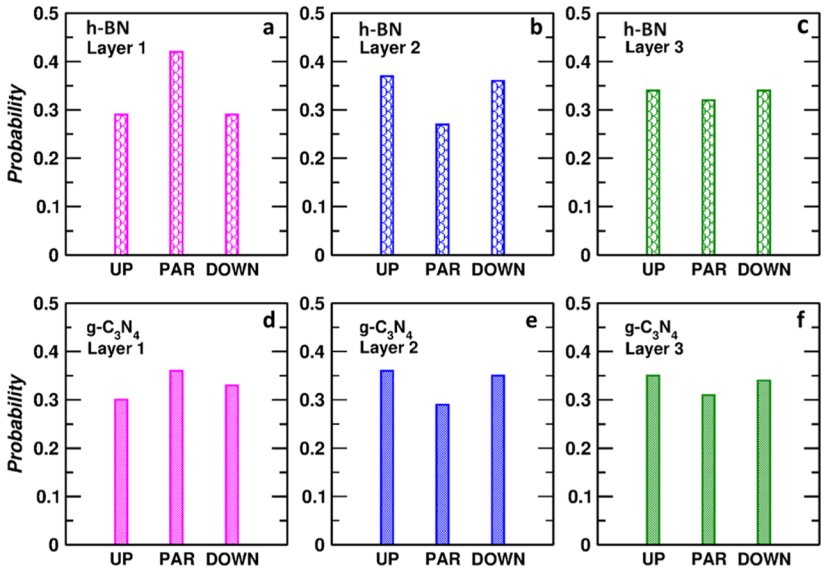

Figure 5. Probability of water molecules in the different layers along the *z*-axis, oriented either "PAR," that is, parallel, or "UP," that is, toward the heterosurface or "DOWN," that is, toward the adjacent layer for (a−c) h-BN-water and (d−f) g−C_3N_4−water systems. The p_z probability is depicted for L1, L2, and L3 in magenta, blue, and green bars for L1, L2, and L3, respectively.

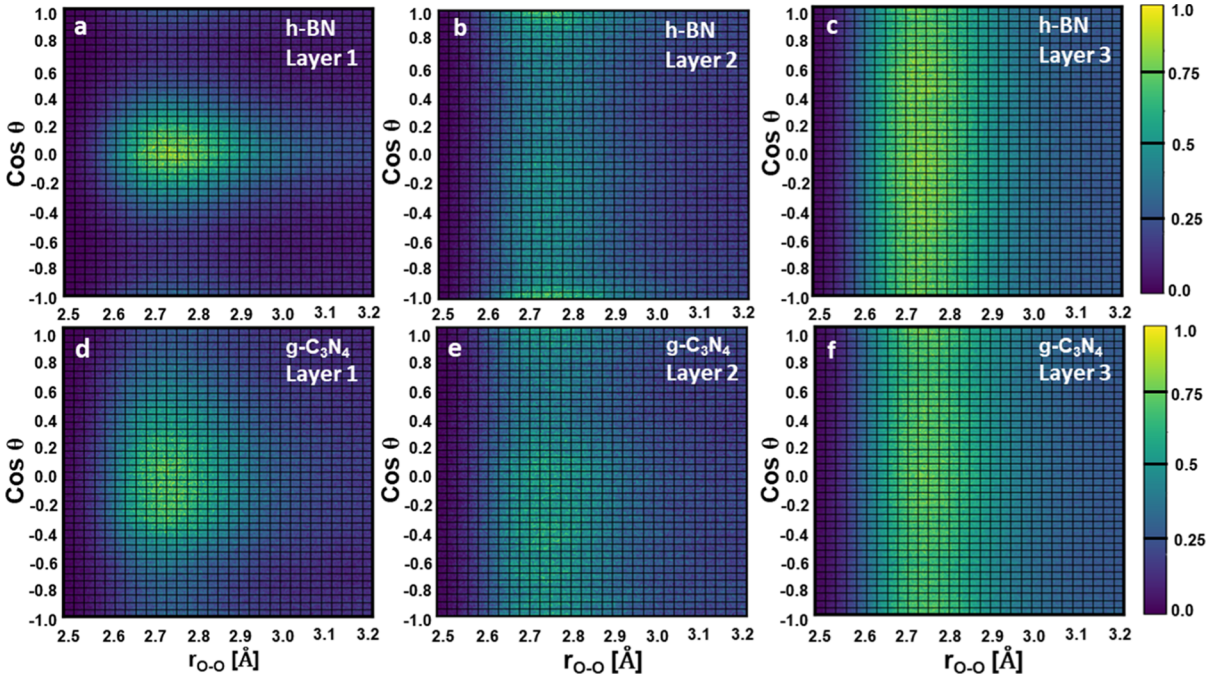

Figure 6. Scatter density plots of the HB patterns formed between the water molecules in layers L1, L2, and L3 from (a−c) h-BN and (d−f) g-C_3N_4. We have O−O distance between a pair of hydrogen-bonded water molecules along the *x*-axis and the cosine of the angle between the O−O vector (donor to acceptor) and the unit normal vector to the surface. The color bar represents the probability (*P*) of finding a correlation between the given O−O distance and angular orientation.

strictly parallel to the instantaneous h-BN surface; however, the O−O distance is more bulklike for g-C_3N_4, and the nonbonded vector is not strictly restricted to the parallel orientation to the surface. It is a known fact that a more hydrophobic system tends to repel the water in contact and hence forms spherical bubbles close to the surface.[81,82] A relatively centered and relatively fanned out cos θ versus r_{O-O} [Å] distribution in the L1 for h-BN and g-C_3N_4, respectively, shows that HBs formed among interfacial water molecules are essentially parallel to the immediate heterosurface. However, the cos θ range is boundless for L2 and L3, and the distribution is uniform. The stern range of cos θ for the h-BN interfacial layer again suggests the unusual hydrogen bonding situation. The most logical explanation that can be drawn from the trend of TOP, HB count, and the orientational features of hydrogen-bonded water molecules is the two-dimensional HBs. Instead of a 3D tetrahedron, the L1 water molecules are arranged in a 2D sheet; the effect is most prominent for h-BN interfacial water molecules. Further investigations are required to determine the order of the 2D hydrogen-bonded structure.

This section highlights the order magnitude of 2D hydrogen-bonded structure among L1, L2, and L3 water

https://doi.org/10.1021/acs.jpcc.2c07098
J. Phys. Chem. C 2023, 127, 2544−2557

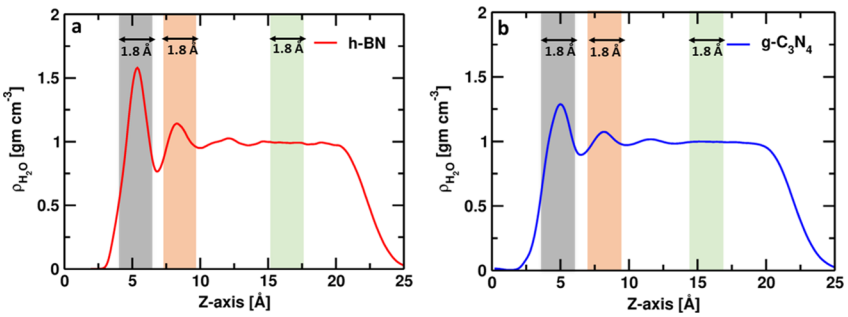

Figure 7. Water density distribution along the top direction (for $z > 0$ Å), and the gray, red, and green patches represent the selected 1.8 Å region chosen from layer 1, layer 2, and layer 3 to study the 2D-HB properties.

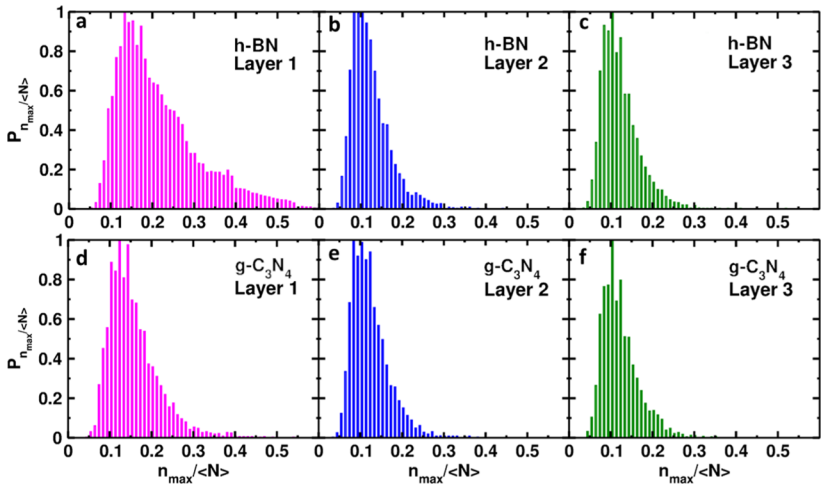

Figure 8. Probability distribution of the $n_{max}/<N>$, where n_{max} and N represent the maximum 2D sheet size attained by water molecules and the total number of water molecules in the chosen section of the (a,d) layer 1 (magenta bars), (b,e) layer 2 (blue bars), and (c,f) layer 3 (green bars) of h-BN and g-C_3N_4.

molecules. Since we are focusing on the 2D-HB sheet structures, a pretested range of 1.80 Å is chosen in each density-defined layer instead of the entire water layer, such that the water molecules lie in the ±0.9 Å from the peak position of the L1 and L2, depicted pictorially in Figure 7.

We started by identifying the water molecules in close contact with each other satisfying the HB criteria, that is, r_{OH} < 2.45 Å and <H−O_{donor}−$O_{acceptor}$ < 30°. Once the paired water molecules forming HBs are recognized, connected component analysis is performed using network graph theory to identify the end-to-end connected water molecules forming a 2D sheet. The maximum number of water molecules forming the largest 2D sheet, termed n_{max}, is obtained from the connected component analysis. Another physically meaningful quantity is N, the total number of water molecules in the chosen 1.80 Å region. Calculations concerning n_{max} and N can provide a statistically meaningful quantity. n_{max} values are obtained by analyzing a 40 ns NVE trajectory, ensuring a proper sampling. The temporal evolution of the absolute n_{max} values is depicted in Figure S4.

Though maximum n_{max}, irrespective of the layer, is distributed in the range 5−10, a significant set of water molecules acquire an extended 2D sheet structure in the L1 of h-BN. Such elongated 2D sheet arrangements are in the L2 and L3 of h-BN and all density-segregated layers of g-C_3N_4. Previous FPMD studies have reported the n_{max} to be 40 in the watervapor interfacial layer;[42] however, this value can change depending on the dimension of the heterosurface. Also, our study involves classical rigid water models, which is why there are fewer extended 2D-HBs in the L1 of h-BN. Since the presenting n_{max} value is not a generic approach, we calculated the probability of $n_{max}/<N>$, where N is the total number of water molecules in the L1 at a given time. From $P_{nmax/<N>}$, depicted in Figure 8, we find a major set of $n_{max}/<N>$ (0.3−0.5) noticeable probability in the L1 of h-BN, which has zero probability for L2 and L3 of h-BN and all layers of g-C_3N_4. For L2 and L3, probability peaks for $n_{max}/<N> \sim 0.1$, irrespective of the surface. The non-zero probability of $n_{max}/<N>$ in the L1 of h-BN, covering the range 0.30 to 0.50, suggests that at a certain time, 33 to 50% of water molecules participate in the 2D-HB formation. Such a phenomenon is absent in other layers of h-BN. A shift in the maximum probability value is observed in the L1 of both heterostructures. Thus, an inherent static property extended 2D-HB and hence the obtained n_{max} are qualified to distinguish between the hydrophobicity of h-BN and g-C_3N_4.

3.4. Hydrogen Bond Dynamics and Translational Diffusion. Our further observations are based on the temporal evolution of the dynamic properties. A correlation between the static and dynamic HB properties can add profoundly to the generalization of the observed hydrophobicity. We calculated the HBLT of water molecules in the different water layers. We computed the lifetime from the continuous hydrogen bond correlation function,[83−87] given as

https://doi.org/10.1021/acs.jpcc.2c07098
J. Phys. Chem. C 2023, 127, 2544−2557

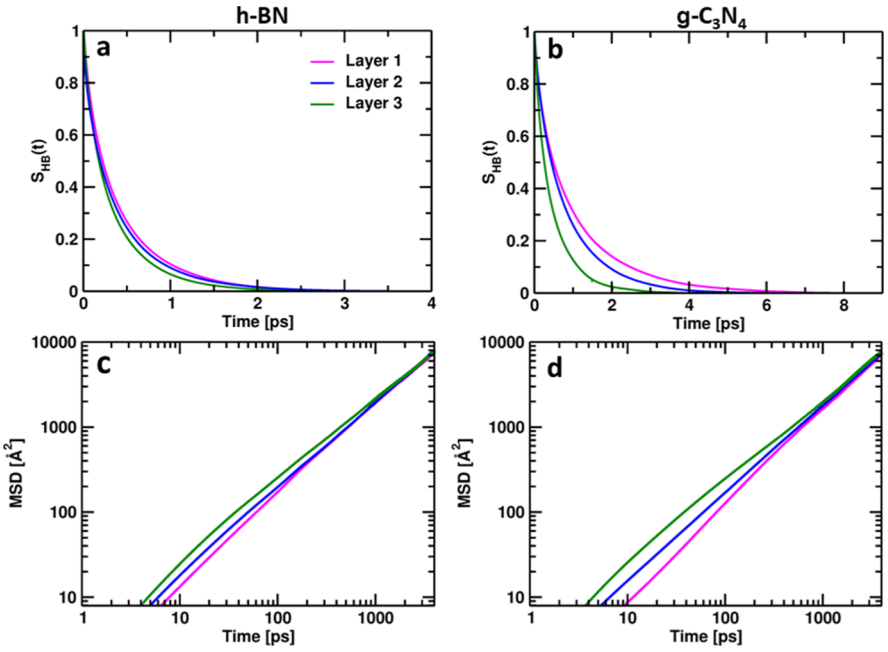

Figure 9. Hydrogen bond lifetime correlation function $S_{HB}(t)$ presented for L1 (magenta line), L2 (blue line), and L3 (green line) water layers for (a) h-BN and (b) g-C_3N_4 systems. The log-log plot of MSD of water molecules in the different density-wise separated layers around (c) h-BN and (d) g-C_3N_4.

$$S_{HB} = \frac{\langle h(0)H(t)\rangle}{\langle h(0)^2\rangle}$$

where $h(t)$ = 1 or 0 depending on whether water molecules follow or do not follow the HB bond and angle criteria, r_{O-H} < 2.45 Å and <H−O−O < 30°, and $H(t)$ = 1 or 0 for a continuously intact HB for time t or otherwise, respectively. The decaying S_{HB} function is provided in Figure 9a,b for h-BN and g-C_3N_4, and the HBLT is obtained by fitting the decaying curve using a monoexponential function $f(x) = A\exp[-(x/\tau_{HB})]$, where τ_{HB} is the average HBLT. The HBLT values are provided in Table 1. The HBLT in the different layers of h-BN is found to be equivalent; however, a decreasing trend is observed for g-C_3N_4 moving from L1 to L3. Thus, in the g-C_3N_4 interfacial layer water−water, HB has greater strength compared to bulk as well as the h-BN interfacial water molecules. The TOP trend[72] shows the noteworthy loss of higher-order q_{tet} for h-BN compared to g-C_3N_4, and we find a comparable trend of HBLT of L1 water molecules surrounding h-BN and g-C_3N_4. Such an observation is expected as the presence of a hydrophobic system induces a defect that leads to a loss of usual tetrahedrality along with the formation of stronger 2D-HB. The h-BN L1 water molecules have faster decaying S_{HB} (τ_{HB} ∼ 0.43 ps) as opposed to g-C_3N_4 (τ_{HB} ∼ 1.01 ps), which can be further correlated with the scattered distribution of O−O distance versus angular orientation of the O−O nonbonded vector. The latter reveals the presence of a slightly elongated distance among hydrogen-bonded O−O pair in the L1 close to h-BN and hence the reduced HBLT compared to g-C_3N_4.

Table 1. Represents the Continuous HB Dynamics and the Diffusion Coefficient Values for Water Molecules in the Different Layers Distributed Along the Normal Direction to H-BN and g-C_3N_4

		S_{HB}		
		a_0	τ_{HB} (ps)	D(m^2 s^{-1})
h-BN	Layer 1	0.88	0.43	3.15 ± 0.03
	Layer 2	0.88	0.41	3.16 ± 0.04
	Layer 3	0.89	0.36	3.23 ± 0.09
g-C_3N_4	Layer 1	0.89	1.01	2.43 ± 0.33
	Layer 2	0.89	0.82	2.36 ± 0.32
	Layer 3	0.89	0.40	2.69 ± 0.41

Following HBLT, we study the translational diffusion coefficient (D), calculated following the MSD of water molecules, given as the following equation

$$D = \lim_{t\to\infty} \frac{\langle |r(t) - r(0)|^2\rangle}{6t} \quad (1)$$

where $r(0)$ and $r(t)$ represent the position of the center of mass of water molecule at times 0 and t respectively. The log−log plot of the MSD is depicted in Figure 9c,d for h-BN and g-C_3N_4, respectively. Hence, the calculated D values along with the standard deviation are provided in Table 1. The standard deviation values are obtained by calculating the MSD of the different sections of the NVE-generated trajectory. The diffusive region is obtained by calculating $\beta(t)$ given as follows

$$\beta(t) = \frac{d\ \ln <\Delta r^2(t)>}{d\ \ln(t)} \quad (2)$$

$\Delta r(t)$ shows the position change with time. As β reaches unity, the section farther is considered for diffusivity calculations. The D values given in m^2 s^{-1} follow the exact trend as HBLT. Fastened decaying S_{HB} leads to a smaller HBLT and a faster diffusion coefficient. The survival interval of water molecules in the L1 is also higher in the g-C_3N_4 compared to h-BN. Hence, the dynamic properties complement each other.

3.5. Anisotropic Decay and Power Spectra. The rotational motion of the water molecules is accounted for by

https://doi.org/10.1021/acs.jpcc.2c07098
J. Phys. Chem. C 2023, 127, 2544−2557

calculating the OACF of the O−H bond vector which determines the temporal evolution of the same. Either first or second-order Legendre polynomial can be used to define the autocorrelation O−H vector. We calculated the OACF of the O_w−H_w vector of water molecules in different layers from the equation,[88]

$$C_2(t) = \langle P_2[u_{OH}(0).\ u_{OH}(t)]\rangle$$

a Legendre polynomial function of rank 2 as the time-dependent polarization anisotropy is allied to the rank 2 rotational function. Here, $u_{OH}(t)$ and $u_{OH}(0)$ represents the OH bond vector at times t and 0, respectively. Hence, the obtained decaying plots are fitted using a stretched monoexponential function $f(x) = A\ \exp\left[-\left(\frac{x}{\tau_2}\right)\right]^{\beta}$, where, parametrization is done for A, a pre-exponential factor, and β, the stretch factor, and the fitting parameters are depicted in Table 2. By fitting the exponentially decaying curves of O−H bond vector orientation in the different layers, depicted in Figure 10a,b for h-BN and g-C_3N_4 affected layers, we find that the L1 water molecules have retarded orientational pace as compared to other layers. Drawing a comparison among interfacial layers of g-C_3N_4 and h-BN, we find a slower reorientation lifetime, that is, 2.69 ps versus 2.20 ps, for water molecules in close interaction of g-C_3N_4. A stronger HB environment may add to the slower reorientation of intramolecular bonds. Relatively weaker HB environment in the h-BN interface resulting due to elongated O−O, the interaction may append the faster orientational dynamics of h-BN. Recent FPMD simulations report a faster dynamic in the interface compared to the bulk. However, the situation alters for FF-based information, which lacks proper polarization and partial charge distribution on the surface. Hence, the observations can be termed circumstantial.

Table 2. Fitting parameters and reorientation lifetimes obtained by fitting a stretched exponential function to the second-order Legendre polynomial curve of OACF

		$C_2(t)$		
		A	τ_2(ps)	β
h-BN	Layer 1	0.81	2.20	0.82
	Layer 2	0.81	1.49	0.82
	Layer 3	0.81	1.32	0.81
g-C3N4	Layer 1	0.80	2.69	0.82
	Layer 2	0.81	1.26	0.82
	Layer 3	0.81	1.10	0.82

The IR spectrum of water molecules consists of libration, intramolecular bending, and stretching in the increasing order of wavenumber. Since we used rigid water, the bending and stretching modes are inaccessible to us, which require the knowledge of intramolecular vibrational modes. Thus, the following discussion proceeds with libration modes related to intramolecular interactions only. The intramolecular interaction of water molecules is usually associated with hydrogen-bonded interactions and networks associated with the peaks centered around low-frequency regions.[89] Experimental studies including far infrared spectroscopy,[90] terahertz spectroscopy,[91] and RAMAN spectroscopy[92,93] dissect the low-frequency region into three separate modes, namely, the libration mode, appearing as the broad peak around 500−700 cm^{-1}; intermolecular stretching among hydrogen bonded O···O, appearing close to 200 cm^{-1}, and intermolecular bending framed as O···O···O, appearing in the 50−60 cm^{-1} range. Recent THz calorimetry identified 450−600 cm^{-1} as the

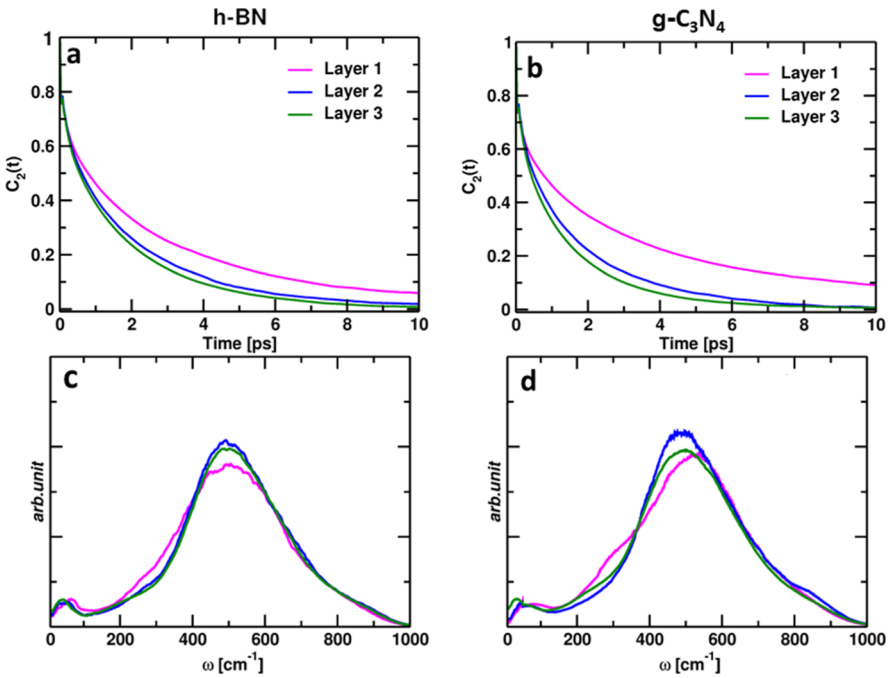

Figure 10. Anisotropically decaying orientation autocorrelation function $C_n(t)$ (n = 2) of OH bond vector of water molecules in layer 1 (magenta line), layer 2 (blue line), and layer 3 (green line) concerning the second-order Legendre polynomial in the three distinct layers around (a) h-BN and (b) g-C_3N_4. (c,d) represents the power spectra of the water molecules obtained from the Fourier transformation of H of water molecules in different layers around h-BN and g-C_3N_4, respectively.

https://doi.org/10.1021/acs.jpcc.2c07098
J. Phys. Chem. C 2023, 127, 2544−2557

libration mode fingerprint.[94] Normalized H_w velocity autocorrelation function component ($C_v^H(t)$) is calculated as = $\frac{\langle \overrightarrow{v_H}(t_0)\overrightarrow{v_H}(t_0+t)\rangle}{\langle \overrightarrow{v_H}(t_0)\cdot\overrightarrow{v_H}(t_0)\rangle}$, where $\overrightarrow{v_H}(t_0)$ and $\overrightarrow{v_H}(t_0+t)$ are the velocity vectors of the H_w atom at times $t_0$and $t_0 + t$, respectively.[89] Fourier transformation of $C_v^H(t)$ results in power spectra. Broad peaks ranging around 0−1000 cm^{-1} are primarily termed libration peaks. As the terminology suggests, the libration peaks are inherently associated with the intermolecular interactions and the orientational motion of the water molecules. The red- and blue-shifted libration peaks are equated to faster and slower orientational and translational dynamics. The local hydrophilicity of g-C_3N_4 induces a familial environment for water molecules. For g-C_3N_4, as depicted in Figure 10d, a blue-shifted libration mode for L1 water molecules sits well with the significantly slowed HBLT and $C_2(t)$ decay compared to L2 and L3/bulk water molecules. Such behavior was reported earlier while comparing nonreactive and reactive flexible FF parameters (FFP).[89] The authors observed a redshift in the libration modes for reactive FFP due to a relaxed environment leading to faster diffusion, slower HBLT, and faster decaying dipole moment orientation. The water molecules in the L1 of the h-BN interface, owing to their hydrophobicity, show faster decaying HB dynamics and smaller reorientation time compared to g-C_3N_4. Hence, the red shift in libration modes is observed. Two other peaks in the low-frequency region centered around 50−60 cm^{-1} and 175−200 cm^{-1} correspond to O-O-O bending modes and O-O/O−H-O stretching modes in tetrahedrally arranged water molecules.[89] For h-BN, the power spectra and the libration modes only differ in intensity as depicted in Figure 10c; however, there is a blueshift in the low-frequency region, 50−60 cm^{-1}, affirming our TOP observation. A lack of proper tetrahedral arrangement leads to frequent O O O bending. For g-C_3N_4, as depicted in Figure 10d, a blueshift was observed in the L1 water molecules; however, the frequency shift in the low-frequency region is inconsequential. The observation can be correlated with the TOP trend and the huge gap in the reorientation lifetime in the different water layers around g-C_3N_4.

4. CONCLUSIONS

We investigated the water affinity of the bilayer heterosurfaces dipped in water by performing the classical molecular dynamics simulation. We analyzed the density-defined layers of water molecules around h-BN and g-C_3N_4, the survival probability of water in layers, and 2D and 3D HB properties. A correlation is drawn among the HB properties, dynamic properties, and hydrophobicity. Comparing both the heterosurface using TOP, we find a relatively greater loss of tetrahedrality in the L1 of h-BN compared to g-C_3N_4; however, the situation altered when we considered the per water HB count and HB-D/A count. Anticipating an anomaly among the L1 water molecules, owing to the difference in the TOP and HB counts, we studied the orientation of the uninterrupted hydrogen bonded water network. Instead of a 3D tetrahedrally arranged hydrogen bonded water structure, we believe the interfacial water molecules are involved in a sheetlike 2D arrangement. The dipole orientation of the water molecules concerning the surface normal vector is calculated to quantify the sheetlike arrangements of HB, and the most probable orientations in the L1 are the ones parallel to the heterosurface. The percentage of the parallel orientation is maximal for h-BN compared to g-C_3N_4. Drawing the correlation amid the distance between the oxygen of hydrogen bonded water pair and the angular orientation of the $O_{donor}-O_{acceptor}$ vector, we find the h-BN L1 water molecules strictly following the near-parallel angular inclination to the immediate surface. However, the situation is not so rigid for g-C_3N_4, where the above-mentioned distribution can acquire a relatively wider range in the allowed hydrogen bonded O−O distance range. A proper distinction for hydrophobicity can be derived based on our mentioned findings. The interconnectedness of these parallelly oriented intermolecular HBs is further studied for L1 water molecules around h-BN and g-C_3N_4. A wide-reaching 2D-HB network is found in the L1 of more hydrophobic h-BN, compared to g-C_3N_4, as the intralayer interaction among water molecules increases to compensate for the defect induced by the hydrorepelling surface. A shift in the maximum probability of $n_{max}/<N>$ in the interfacial layer demonstrates an extended 2D-HB network. Further correlations are drawn among temporally evolving dynamic properties and static hydrogen bonding properties. The $L1_{g\text{-}C3N4}$ water molecules have a τ_{HB} = 1.01 ps representing a longer continuous hydrogen-bonded state among the interfacial water molecules as opposed to $L1_{h-BN}$ water molecules (τ_{HB} = 0.43 ps). Elongated O−O interaction distance leads to a relatively weaker HB environment in the h-BN interface resulting in faster orientational dynamics of the h-BN (τ_2 = 2.20 ps) compared to g-C_3N_4($\boldsymbol{\tau_2 = 2.69}$ **ps**). The current discussion blends the structural, dynamic, spectral, and instantaneous HB phenomenon to shed light on how water behavior can be distinguished near a hydrophobic or amphiphilic surface. We believe this study unsheathes a better understanding of heterosurface hydrophobicity and can be referred for future investigations.

■ ASSOCIATED CONTENT

Supporting Information

The Supporting Information is available free of charge at https://pubs.acs.org/doi/10.1021/acs.jpcc.2c07098.

Description about the structure of water layers, probability distribution, n_{max} of hydrogen-bonded water molecules, figures, and coordinates of the systems (PDF)

■ AUTHOR INFORMATION

Corresponding Author

Bhabani S. Mallik − *Department of Chemistry, Indian Institute of Technology Hyderabad, Sangareddy 502285 Telangana, India;* orcid.org/0000-0001-9657-1497; Phone: +91 40 2301 6258; Email: bhabani@chy.iith.ac.in

Author

Adyasa Priyadarsini − *Department of Chemistry, Indian Institute of Technology Hyderabad, Sangareddy 502285 Telangana, India*

Complete contact information is available at: https://pubs.acs.org/10.1021/acs.jpcc.2c07098

Notes

The authors declare no competing financial interest.

https://doi.org/10.1021/acs.jpcc.2c07098
J. Phys. Chem. C 2023, 127, 2544−2557

■ ACKNOWLEDGMENTS

Adyasa Priyadarsini likes to thank the Ministry of Education, India, for providing the Ph.D. fellowship.

■ REFERENCES

(1) Tan, C.; Cao, X.; Wu, X.-J.; He, Q.; Yang, J.; Zhang, X.; Chen, J.; Zhao, W.; Han, S.; Nam, G.-H.; Sindoro, M.; Zhang, H. Recent Advances in Ultrathin Two-Dimensional Nanomaterials. *Chem. Rev.* **2017**, *117*, 6225−6331.

(2) Cao, Y.; Maitarad, P.; Gao, M.; Taketsugu, T.; Li, H.; Yan, T.; Shi, L.; Zhang, D. Defect-Induced Efficient Dry Reforming of Methane over Two-Dimensional Ni/h-Boron Nitride Nanosheet Catalysts. *Appl. Catal. B* **2018**, *238*, 51−60.

(3) Deng, D.; Novoselov, K. S.; Fu, Q.; Zheng, N.; Tian, Z.; Bao, X. Catalysis with Two-Dimensional Materials and Their Heterostructures. *Nat. Nanotechnol* **2016**, *11*, 218−230.

(4) Dean, C. R.; Young, A. F.; Meric, I.; Lee, C.; Wang, L.; Sorgenfrei, S.; Watanabe, K.; Taniguchi, T.; Kim, P.; Shepard, K. L.; Hone, J. Boron Nitride Substrates for High-Quality Graphene Electronics. *Nature Nanotech* **2010**, *5*, 722−726.

(5) Yoo, E.; Kim, J.; Hosono, E.; Zhou, H.; Kudo, T.; Honma, I. Large Reversible Li Storage of Graphene Nanosheet Families for Use in Rechargeable Lithium Ion Batteries. *Nano Lett* **2008**, *8*, 2277−2282.

(6) Sun, Y.; Gao, S.; Xie, Y. Atomically-Thick Two-Dimensional Crystals: Electronic Structure Regulation and Energy Device Construction. *Chem. Soc. Rev.* **2013**, *43*, 530−546.

(7) Peng, X.; Peng, L.; Wu, C.; Xie, Y. Two Dimensional Nanomaterials for Flexible Supercapacitors. *Chem. Soc. Rev.* **2014**, *43*, 3303−3323.

(8) Britnell, L.; Gorbachev, R. V.; Jalil, R.; Belle, B. D.; Schedin, F.; Katsnelson, M. I.; Eaves, L.; Morozov, S. V.; Mayorov, A. S.; Peres, N. M. R.; Castro Neto, A. H.; Leist, J.; Geim, A. K.; Ponomarenko, L. A.; Novoselov, K. S. Electron Tunneling through Ultrathin Boron Nitride Crystalline Barriers. *Nano Lett* **2012**, *12*, 1707−1710.

(9) Yang, S.; Gong, Y.; Zhang, J.; Zhan, L.; Ma, L.; Fang, Z.; Vajtai, R.; Wang, X.; Ajayan, P. M. Exfoliated Graphitic Carbon Nitride Nanosheets as Efficient Catalysts for Hydrogen Evolution Under Visible Light. *Adv Mater* **2013**, *25*, 2452−2456.

(10) Wang, L.; Hu, Y.; Qi, F.; Ding, L.; Wang, J.; Zhang, X.; Liu, Q.; Liu, L.; Sun, H.; Qu, P. Anchoring Black Phosphorus Nanoparticles onto ZnS Porous Nanosheets: Efficient Photocatalyst Design and Charge Carrier Dynamics. *ACS Appl. Mater. Interfaces* **2020**, *12*, 8157−8167.

(11) Zheng, L.; Ye, X.; Deng, X.; Wang, Y.; Zhao, Y.; Shi, X.; Zheng, H. Black Phosphorus Quantum Dot-Sensitized TiO2 Nanotube Arrays with Enriched Oxygen Vacancies for Efficient Photoelectrochemical Water Splitting. *ACS Sustainable Chem. Eng.* **2020**, *8*, 15906−15914.

(12) Bhunia, M. K.; Yamauchi, K.; Takanabe, K. Harvesting Solar Light with Crystalline Carbon Nitrides for Efficient Photocatalytic Hydrogen Evolution. *Angew. Chem. Int. Ed* **2014**, *53*, 11001−11005.

(13) Yi, J.; El-Alami, W.; Song, Y.; Li, H.; Ajayan, P. M.; Xu, H. Emerging Surface Strategies on Graphitic Carbon Nitride for Solar Driven Water Splitting. *Chem. Eng. J.* **2020**, *382*, 122812.

(14) Li, X.; Zhao, J.; Yang, J. Semihydrogenated BN Sheet: A Promising Visible-Light Driven Photocatalyst for Water Splitting. *Sci Rep* **2013**, *3*, 1858.

(15) Wang, G.; Zhi, Y.; Bo, M.; Xiao, S.; Li, Y.; Zhao, W.; Li, Y.; Li, Y.; He, Z. 2D Hexagonal Boron Nitride/Cadmium Sulfide Heterostructure as a Promising Water-Splitting Photocatalyst. *Phys. Status Solidi B* **2020**, *257*, 1900431.

(16) Brown, P. S.; Bhushan, B. Durable, Superoleophobic Polymer−Nanoparticle Composite Surfaces with Re-Entrant Geometry via Solvent-Induced Phase Transformation. *Sci Rep* **2016**, *6*, 21048.

(17) Papierowska, E.; Szporak-Wasilewska, S.; Szewińska, J.; Szatyłowicz, J.; Debaene, G.; Utratna, M. Contact Angle Measurements and Water Drop Behavior on Leaf Surface for Several Deciduous Shrub and Tree Species from a Temperate Zone. *Trees* **2018**, *32*, 1253−1266.

(18) Khan, M. Q.; Kharaghani, D.; Nishat, N.; Shahzad, A.; Hussain, T.; Khatri, Z.; Zhu, C.; Kim, I. S. Preparation and Characterizations of Multifunctional PVA/ZnO Nanofibers Composite Membranes for Surgical Gown Application. *J. Mater. Res. Technol.* **2019**, *8*, 1328−1334.

(19) Li, X.; Qiu, H.; Liu, X.; Yin, J.; Guo, W. Wettability of Supported Monolayer Hexagonal Boron Nitride in Air. *Adv. Funct. Mater.* **2017**, *27*, 1603181.

(20) Teng, Z.; Yang, N.; Lv, H.; Wang, S.; Hu, M.; Wang, C.; Wang, D.; Wang, G. Edge-Functionalized g-C3N4 Nanosheets as a Highly Efficient Metal-Free Photocatalyst for Safe Drinking Water. *Chem* **2019**, *5*, 664−680.

(21) Shin, Y. J.; Wang, Y.; Huang, H.; Kalon, G.; Wee, A. T. S.; Shen, Z.; Bhatia, C. S.; Yang, H. Surface-Energy Engineering of Graphene. *Langmuir* **2010**, *26*, 3798−3802.

(22) Eichler, J.; Lesniak, C. Boron Nitride (BN) and BN Composites for High-Temperature Applications. *J. Eur. Ceram. Soc.* **2008**, *28*, 1105−1109.

(23) Singh, B.; Kaur, G.; Singh, P.; Singh, K.; Kumar, B.; Vij, A.; Kumar, M.; Bala, R.; Meena, R.; Singh, A.; Thakur, A.; Kumar, A. Nanostructured Boron Nitride With High Water Dispersibility For Boron Neutron Capture Therapy. *Sci Rep* **2016**, *6*, 35535.

(24) Fang, H.; Bai, S.-L.; Wong, C. P. White Graphene" − Hexagonal Boron Nitride Based Polymeric Composites and Their Application in Thermal Management. *Compos. Commun* **2016**, *2*, 19−24.

(25) Wagemann, E.; Wang, Y.; Das, S.; Mitra, S. K. On the Wetting Translucency of Hexagonal Boron Nitride. *Phys. Chem. Chem. Phys.* **2020**, *22*, 7710−7718.

(26) Li, H.; Zeng, X. C. Wetting and Interfacial Properties of Water Nanodroplets in Contact with Graphene and Monolayer Boron−Nitride Sheets. *ACS Nano* **2012**, *6*, 2401−2409.

(27) Lv, Y.; Chen, S.; Shen, Y.; Ji, J.; Zhou, Q.; Liu, S.; Zhang, Y. Competitive Multiple-Mechanism-Driven Electrochemiluminescent Detection of 8-Hydroxy-2′-Deoxyguanosine. *J. Am. Chem. Soc.* **2018**, *140*, 2801−2804.

(28) Lu, Q.; Deng, J.; Hou, Y.; Wang, H.; Li, H.; Zhang, Y. One-Step Electrochemical Synthesis of Ultrathin Graphitic Carbon Nitride Nanosheets and Their Application to the Detection of Uric Acid. *Chem. Commun.* **2015**, *51*, 12251−12253.

(29) Barrio, J.; Shalom, M. Rational Design of Carbon Nitride Materials by Supramolecular Preorganization of Monomers. *ChemCatChem* **2018**, *10*, 5573−5586.

(30) Zou, J.; Yu, Y.; Qiao, K.; Wu, S.; Yan, W.; Cheng, S.; Jiang, N.; Wang, J. Microwave Synthesis of Phosphorus-Doped Graphitic Carbon Nitride Nanosheets with Enhanced Electrochemiluminescence Signals. *J Mater Sci* **2020**, *55*, 13618−13633.

(31) Argyris, D.; Tummala, N. R.; Striolo, A.; Cole, D. R. Molecular Structure and Dynamics in Thin Water Films at the Silica and Graphite Surfaces. *J. Phys. Chem. C* **2008**, *112*, 13587−13599.

(32) Argyris, D.; Cole, D. R.; Striolo, A. Dynamic Behavior of Interfacial Water at the Silica Surface. *J. Phys. Chem. C* **2009**, *113*, 19591−19600.

(33) Argyris, D.; Ho, T.; Cole, D. R.; Striolo, A. Molecular Dynamics Studies of Interfacial Water at the Alumina Surface. *J. Phys. Chem. C* **2011**, *115*, 2038−2046.

(34) Phan, A.; Ho, T. A.; Cole, D. R.; Striolo, A. Molecular Structure and Dynamics in Thin Water Films at Metal Oxide Surfaces: Magnesium, Aluminum, and Silicon Oxide Surfaces. *J. Phys. Chem. C* **2012**, *116*, 15962−15973.

(35) Kessler, J.; Elgabarty, H.; Spura, T.; Karhan, K.; Partovi-Azar, P.; Hassanali, A. A.; Kühne, T. D. Structure and Dynamics of the Instantaneous Water/Vapor Interface Revisited by Path-Integral and Ab Initio Molecular Dynamics Simulations. *J. Phys. Chem. B* **2015**, *119*, 10079−10086.

(36) Willard, A. P.; Chandler, D. Instantaneous Liquid Interfaces. *J. Phys. Chem. B* **2010**, *114*, 1954−1958.

https://doi.org/10.1021/acs.jpcc.2c07098
J. Phys. Chem. C 2023, 127, 2544−2557

(37) Giberti, F.; Hassanali, A. A. The Excess Proton at the Air-Water Interface: The Role of Instantaneous Liquid Interfaces. *J. Chem. Phys.* **2017**, *146*, 244703.
(38) Zhang, C.; Knyazev, D. G.; Vereshaga, Y. A.; Ippoliti, E.; Nguyen, T. H.; Carloni, P.; Pohl, P. Water at Hydrophobic Interfaces Delays Proton Surface-to-Bulk Transfer and Provides a Pathway for Lateral Proton Diffusion. *Proc Natl Acad Sci U S A* **2012**, *109*, 9744−9749.
(39) Tarbuck, T. L.; Ota, S. T.; Richmond, G. L. Spectroscopic Studies of Solvated Hydrogen and Hydroxide Ions at Aqueous Surfaces. *J. Am. Chem. Soc.* **2006**, *128*, 14519−14527.
(40) Medders, G. R.; Paesani, F. Dissecting the Molecular Structure of the Air/Water Interface from Quantum Simulations of the Sum-Frequency Generation Spectrum. *J. Am. Chem. Soc.* **2016**, *138*, 3912−3919.
(41) Ni, Y.; Skinner, J. L. Communication: Vibrational Sum-Frequency Spectrum of the Air-Water Interface, Revisited. *J. Chem. Phys.* **2016**, *145*, 031103.
(42) Pezzotti, S.; Galimberti, D. R.; Gaigeot, M.-P. 2D H-Bond Network as the Topmost Skin to the Air−Water Interface. *J. Phys. Chem. Lett.* **2017**, *8*, 3133−3141.
(43) Adhikari, S.; Kusaka, R.; Inoue, K.; Adhikari, A.; Yamaguchi, S.; Tahara, T. Accurate Determination of Complex $\chi(2)$ Spectrum of the Air/Water Interface. *J. Chem. Phys.* **2015**, *143*, 124707.
(44) Yamaguchi, S. Comment on "Phase Reference in Phase-Sensitive Sum-Frequency Vibrational Spectroscopy". *J. Chem. Phys.J. Chem. Phys.* **20162016**, *145*, 167101.
(45) Priyadarsini, A.; Mallik, B. S. Amphiphilicity of Intricate Layered Graphene/g-C3N4 Nanosheets. *J. Phys. Chem. B* **2021**, *125*, 11697−11708.
(46) Priyadarsini, A.; Mallik, B. S. Aqueous Affinity and Interfacial Dynamics of Anisotropic Buckled Black Phosphorous. *J. Phys. Chem. B* **2021**, *125*, 7527−7536.
(47) Rafiee, J.; Mi, X.; Gullapalli, H.; Thomas, A. V.; Yavari, F.; Shi, Y.; Ajayan, P. M.; Koratkar, N. A. Wetting Transparency of Graphene. *Nat. Mater.* **2012**, *11*, 217−222.
(48) Wei, N.; Lv, C.; Xu, Z. Wetting of Graphene Oxide: A Molecular Dynamics Study. *Langmuir* **2014**, *30*, 3572−3578.
(49) Xu, K.; Zhang, J.; Hao, X.; Zhang, C.; Wei, N.; Zhang, C. Wetting Properties of Defective Graphene Oxide: A Molecular Simulation Study. *Molecules* **2018**, *23*, 1439.
(50) Tang, F.; Ohto, T.; Sun, S.; Rouxel, J. R.; Imoto, S.; Backus, E. H. G.; Mukamel, S.; Bonn, M.; Nagata, Y. Molecular Structure and Modeling of Water−Air and Ice−Air Interfaces Monitored by Sum-Frequency Generation. *Chem. Rev.* **2020**, *120*, 3633−3667.
(51) Smirnov, K. S. A Molecular Dynamics Study of the Interaction of Water with the External Surface of Silicalite-1. *Phys. Chem. Chem. Phys.* **2017**, *19*, 2950−2960.
(52) Priyadarsini, A.; Mallik, B. S. Aqueous Affinity and Interfacial Dynamics of Anisotropic Buckled Black Phosphorous. *J. Phys. Chem. B* **2021**, *125*, 7527−7536.
(53) Willard, A. P.; Chandler, D. Instantaneous Liquid Interfaces. *J. Phys. Chem. B* **2010**, *114*, 1954−1958.
(54) Pezzotti, S.; Serva, A.; Sebastiani, F.; Brigiano, F. S.; Galimberti, D. R.; Potier, L.; Alfarano, S.; Schwaab, G.; Havenith, M.; Gaigeot, M.-P. Molecular Fingerprints of Hydrophobicity at Aqueous Interfaces from Theory and Vibrational Spectroscopies. *J. Phys. Chem. Lett.* **2021**, *12*, 3827−3836.
(55) Plimpton, S. Fast Parallel Algorithms for Short-Range Molecular Dynamics. *J. Comput. Phys* **1995**, *117*, 1−19.
(56) Wang, J.; Wolf, R. M.; Caldwell, J. W.; Kollman, P. A.; Case, D. A. Development and Testing of a General Amber Force Field. *J. Comput. Chem.* **2004**, *25*, 1157−1174.
(57) Wang, J.; Wang, W.; Kollman, P. A.; Case, D. A. Automatic Atom Type and Bond Type Perception in Molecular Mechanical Calculations. *J. Mol. Graph.* **2006**, *25*, 247−260.
(58) Jorgensen, W. L.; Tirado-Rives, J. The OPLS [Optimized Potentials for Liquid Simulations] Potential Functions for Proteins, Energy Minimizations for Crystals of Cyclic Peptides and Crambin. *J. Am. Chem. Soc.* **1988**, *110*, 1657−1666.
(59) Jorgensen, W. L.; Maxwell, D. S.; Tirado-Rives, J. Development and Testing of the OPLS All-Atom Force Field on Conformational Energetics and Properties of Organic Liquids. *J. Am. Chem. Soc.* **1996**, *118*, 11225−11236.
(60) Tersoff, J. New Empirical Approach for the Structure and Energy of Covalent Systems. *Phys. Rev. B* **1988**, *37*, 6991−7000.
(61) Tersoff, J. Modeling Solid-State Chemistry: Interatomic Potentials for Multicomponent Systems. *Phys. Rev. B* **1989**, *39*, 5566−5568.
(62) Berendsen, H. J. C.; Grigera, J. R.; Straatsma, T. P. The Missing Term in Effective Pair Potentials. *J. Phys. Chem.* **1987**, *91*, 6269−6271.
(63) Mayo, S. L.; Olafson, B. D.; Goddard, W. A. DREIDING: A Generic Force Field for Molecular Simulations. *J. Phys. Chem.* **1990**, *94*, 8897−8909.
(64) Won, C. Y.; Aluru, N. R. Water Permeation through a Subnanometer Boron Nitride Nanotube. *J. Am. Chem. Soc.* **2007**, *129*, 2748−2749.
(65) Liu, Y.; Xie, D.; Song, M.; Jiang, L.; Fu, G.; Liu, L.; Li, J. Water Desalination across Multilayer Graphitic Carbon Nitride Membrane: Insights from Non-Equilibrium Molecular Dynamics Simulations. *Carbon* **2018**, *140*, 131−138.
(66) Kolafa, J.; Nezbeda, I.; Pavlíček, J.; Smith, W. R. Global Phase Diagrams of Model and Real Binary Fluid Mixtures: Lorentz−Berthelot Mixture of Attractive Hard Spheres. *Fluid Phase Equilib* **1998**, *146*, 103−121.
(67) Zarkova, L.; Hohm, U.; Damyanova, M. Comparison of Lorentz−Berthelot and Tang−Toennies Mixing Rules Using an Isotropic Temperature-Dependent Potential Applied to the Thermo-physical Properties of Binary Gas Mixtures of CH4, CF4, SF6, and C(CH3)4 with Ar, Kr, and Xe. *Int. J. Thermophys.* **2004**, *25*, 1775−1798.
(68) Nosé, S. A Unified Formulation of the Constant Temperature Molecular Dynamics Methods. *J. Chem. Phys.* **1984**, *81*, 511−519.
(69) Hoover, W. G. Canonical Dynamics: Equilibrium Phase-Space Distributions. *Phys. Rev. A* **1985**, *31*, 1695−1697.
(70) Martyna, G. J.; Klein, M. L.; Tuckerman, M. Nosé−Hoover Chains: The Canonical Ensemble via Continuous Dynamics. *J. Chem. Phys.* **1992**, *97*, 2635−2643.
(71) Ryckaert, J.-P.; Ciccotti, G.; Berendsen, H. J. C. Numerical Integration of the Cartesian Equations of Motion of a System with Constraints: Molecular Dynamics of n-Alkanes. *J. Comput. Phys* **1977**, *23*, 327−341.
(72) Errington, J. R.; Debenedetti, P. G. Relationship between Structural Order and the Anomalies of Liquid Water. *Nature* **2001**, *409*, 318−321.
(73) Torquato, S.; Truskett, T. M.; Debenedetti, P. G. Is Random Close Packing of Spheres Well Defined? *Phys. Rev. Lett.* **2000**, *84*, 2064−2067.
(74) Truskett, T. M.; Torquato, S.; Debenedetti, P. G. Towards a Quantification of Disorder in Materials: Distinguishing Equilibrium and Glassy Sphere Packings. *Phys. Rev. E* **2000**, *62*, 993−1001.
(75) Duboué-Dijon, E.; Laage, D. Characterization of the Local Structure in Liquid Water by Various Order Parameters. *J. Phys. Chem. B* **2015**, *119*, 8406−8418.
(76) Gaiduk, A. P.; Gygi, F.; Galli, G. Density and Compressibility of Liquid Water and Ice from First-Principles Simulations with Hybrid Functionals. *J. Phys. Chem. Lett.* **2015**, *6*, 2902−2908.
(77) Kessler, J.; Elgabarty, H.; Spura, T.; Karhan, K.; Partovi-Azar, P.; Hassanali, A. A.; Kühne, T. D. Structure and Dynamics of the Instantaneous Water/Vapor Interface Revisited by Path-Integral and Ab Initio Molecular Dynamics Simulations. *J. Phys. Chem. B* **2015**, *119*, 10079−10086.
(78) Kayal, A.; Chandra, A. Water in Confinement between Nanowalls: Results for Hexagonal Boron Nitride versus Graphene Sheets from Ab Initio Molecular Dynamics. *J. Phys. Chem. C* **2019**, *123*, 6130−6140.

(79) Aspera, S. M.; David, M.; Kasai, H. First-Principles Study of the Adsorption of Water on Tri-s-Triazine-Based Graphitic Carbon Nitride. *Jpn. J. Appl. Phys.* **2010**, *49*, 115703.
(80) Xu, J.; Antonietti, M. The Performance of Nanoparticulate Graphitic Carbon Nitride as an Amphiphile. *J. Am. Chem. Soc.* **2017**, *139*, 6026−6029.
(81) Lazar, P.; Otyepková, E.; Pykal, M.; Čépe, K.; Otyepka, M. Role of the Puckered Anisotropic Surface in the Surface and Adsorption Properties of Black Phosphorus. *Nanoscale* **2018**, *10*, 8979−8988.
(82) Zhao, J.; Zhu, J.; Cao, R.; Wang, H.; Guo, Z.; Sang, D. K.; Tang, J.; Fan, D.; Li, J.; Zhang, H. Liquefaction of Water on the Surface of Anisotropic Two-Dimensional Atomic Layered Black Phosphorus. *Nat. Commun.* **2019**, *10*, 4062.
(83) Luzar, A. Water Hydrogen-Bond Dynamics Close to Hydrophobic and Hydrophilic Groups. *Faraday Discuss* **1996**, *103*, 29−40.
(84) Luzar, A.; Chandler, D. Effect of Environment on Hydrogen Bond Dynamics in Liquid Water. *Phys. Rev. Lett.* **1996**, *76*, 928−931.
(85) Luzar, A. Resolving the Hydrogen Bond Dynamics Conundrum. *J. Chem. Phys.* **2000**, *113*, 10663−10675.
(86) Chandra, A. Effects of Ion Atmosphere on Hydrogen-Bond Dynamics in Aqueous Electrolyte Solutions. *Phys. Rev. Lett.* **2000**, *85*, 768−771.
(87) Balasubramanian, S.; Pal, S.; Bagchi, B. Hydrogen-Bond Dynamics near a Micellar Surface: Origin of the Universal Slow Relaxation at Complex Aqueous Interfaces. *Phys. Rev. Lett.* **2002**, *89*, 115505.
(88) Kumar, P.; Franzese, G.; Buldyrev, S. V.; Stanley, H. E. Molecular Dynamics Study of Orientational Cooperativity in Water. *Phys Rev E Stat Nonlin Soft Matter Phys* **2006**, *73*, 041505.
(89) Prasad, D.; Mitra, N.; Bandyopadhyay, S. Intermolecular Dynamics of Water: Suitability of Reactive Interatomic Potential. *J. Phys. Chem. B* **2019**, *123*, 6529−6535.
(90) Hasted, J. B.; Husain, S. K.; Frescura, F. A. M.; Birch, J. R. Far-Infrared Absorption in Liquid Water. *Chem. Phys. Lett.* **1985**, *118*, 622−625.
(91) Thrane, L.; Jacobsen, R. H.; Uhd Jepsen, P.; Keiding, S. R. THz Reflection Spectroscopy of Liquid Water. *Chem. Phys. Lett.* **1995**, *240*, 330−333.
(92) Walrafen, G. E. Raman Spectral Studies of Water Structure. *J. Chem. Phys.* **1964**, *40*, 3249−3256.
(93) Krishnamurthy, S.; Bansil, R.; Wiafe-Akenten, J. Low-frequency Raman Spectrum of Supercooled Water. *J. Chem. Phys.* **1983**, *79*, 5863−5870.
(94) Pezzotti, S.; Sebastiani, F.; van Dam, E. P.; Ramos, S.; Conti Nibali, V.; Schwaab, G.; Havenith, M. Spectroscopic Fingerprints of Cavity Formation and Solute Insertion as a Measure of Hydration Entropic Loss and Enthalpic Gain. *Angew. Chem. Int. Ed.* **2022**, *61*, No. e202203893.

https://doi.org/10.1021/acs.jpcc.2c07098
J. Phys. Chem. C 2023, 127, 2544−2557